# Supplement

…

## 2 Materials and methodologies

### 2.1 ORS-CT and beam geometry

The area of the test field is 40 m × 40 m. open-path TDL is used as the ORS analyzer, which is installed on a scanner and aims at multiple retroreflectors by scanning periodically and continuously. To compare with the results of GT-MG algorithm, we used an overlapping beam configuration similar to the one used in Verkruysse and Todd (2005). As shown in Fig. 1, four TDL analyzers are located at the four corners of the test field. The retroreflectors are evenly distributed along the edges of the field. The total number of retroreflectors is 20. Each retroreflector reflects the laser beams coming from two different directions. Neglecting the overlapped beams along the diagonals, total beam number is 38. For traditional pixel-based algorithm, the pixel number should be no more than the beam number. Therefore, we divide the test field into 6 × 6 = 36 pixels. The concentration within each pixel is assumed to be uniform.

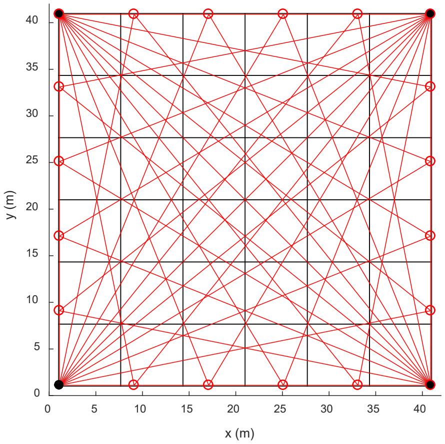

**Figure 1.** The beam configuration and grid division. The field is divided into 6 × 6 grid pixels. Four open-path TDL analyzers locate at four corners. 20 retroreflectors are distributed on the edges of the field.

For each laser beam, the path-integrated concentration (PIC) is measured by the analyzer. The predicated PIC for one beam equals to the sum of the multiplication of the pixel concentration and the length of the beam inside the pixel. In generality, let us assume that the site is divided into $N_c = m \times n$ pixels, which are arranged as a vector according to the left-to-right and top-to-bottom sequence and indexed by $j$. The average concentration for $j$-th pixel is $c_j$. The total number of laser beams is $N_b$ which are indexed by $i$. The length of the $i$-th laser beam inside the $j$-th pixel is $L_{ij}$. Then for the $i$-th beam, the measured PIC $b_i$ is contributed by all the pixels. We have the following linear equation

$$b_i = \sum_{j=1}^{N_c} L_{ij} c_j \tag{1}$$

A system of linear equations can be set up for all the beams

$$\boldsymbol{b} = \boldsymbol{Lc} \tag{2}$$

where $\boldsymbol{L}$ is the kernel matrix that incorporates the specific beam geometry with the pixel dimensions, $\boldsymbol{c}$ is the unknown concentration vector of the pixels, $\boldsymbol{b}$ is a vector of the measured PIC data. Using least square approach, the reconstruction is to minimize the following problem

$$\min_{\boldsymbol{c}} \ ||\boldsymbol{Lc} - \boldsymbol{b}||_2^2, \text{ subject to } \boldsymbol{c} \geq 0 \tag{3}$$

where $||\cdot||_2$ denotes the Euclidean norm. This non-negative constrained linear least square problem can be solved by the widely used NNLS optimization algorithm (Lawson and Janson, 1995), which is an active-set optimization method using an iterative procedure to converge to the best fit of positive values. The realization in MATLAB software as the routine "lsqnonneg" was used in this study. The optimal least square solution is not smooth because the minimizing process does not introduce smooth *a priori* information. In this paper, the "NNLS algorithm" to the tomographic reconstruction refers to solve the original problem using the NNLS optimization algorithm without adding additional *a priori* information. When the system of linear equations is underdetermined, the solution is not unique. Additional information needs to be introduced to choose the appropriate solution.

### 2.2 LTD algorithm and Tikhonov regularization

The LTD algorithm introduces the smoothness *a priori* information through setting the third-order derivative of the concentration to be zero at each pixel in both $x$ and $y$ directions, which will generate solutions that are locally quadratic (Price et al., 2001). We have defined $c_j$ as an element of one-dimensional (1-D) concentration vector of the pixels, but the pixels also have two-dimensional (2-D) structure according to the grid division of the site area and can be indexed by the row number $k$ and column number $l$, where $j=(k-1)n+l$. We use $C_{k,l}$ denotes the pixel concentration at pixel located at $k$-th row and $l$-th column of the grids. The third-derivative prior equations at ($k$, $l$) pixel is define as

$$\frac{d^3C}{dx^3} = (C_{k+2,l} - 3C_{k+1,l} + 3C_{k,l} - C_{k-1,l})\frac{1}{\Delta d} = 0$$

$$\frac{d^3C}{dy^3} = (C_{k,l+2} - 3C_{k,l+1} + 3C_{k,l} - C_{k,l-1})\frac{1}{\Delta d} = 0 \tag{4}$$

where $\Delta d=\Delta x=\Delta y$ is the grid length in $x$, $y$ direction. Therefore, two additional linear equations are introduced at each pixel defined by Eq. (4). There will be $2N_c$ linear equations appended to the original linear equations defined by Eq. (2), resulting in a new over-determined system of linear equations which has $(2N_c + N_b)$ equations and $N_c$ unknowns.

A weight needs to be assigned to each equation depending on the uncertainty of the observation. Assuming the analyzers have the same performance, the uncertainty is mainly related to the path length. Therefore, equations are assigned weights inversely proportional to path length to make sure different paths have equal influences. In this study, the lengths of the laser paths are approximately equal to each other. So their weights were set to be the same value and scaled to be 1. The weights for the third-derivative prior equations were assigned to be the same value of $w$ because they were all based on the same grid length. The determination of $w$ follows the scheme of determining the regularization parameter described in the following text. Using least square approach, the reconstruction is to minimize the following problem

$$\min_{\boldsymbol{c}} \left\| \begin{bmatrix} \boldsymbol{L} \\ w\boldsymbol{T} \end{bmatrix} \boldsymbol{c} - \begin{bmatrix} \boldsymbol{b} \\ 0 \end{bmatrix} \right\|_2^2, \text{ subject to } \boldsymbol{c} \geq 0 \tag{5}$$

where $\boldsymbol{T}$ is the kernel matrix for the third-derivative prior equations. Assuming the new augmented kernel matrix is $\boldsymbol{A}$, observation vector is $\boldsymbol{p}$, then the new system of linear equations is $\boldsymbol{Ac}=\boldsymbol{p}$. The non-negative least square solution was also found by the NNLS optimization algorithm. If the non-negative constrains are ignored, the least square solution can be found analytically as $\hat{\boldsymbol{c}} = (\boldsymbol{A}^{\boldsymbol{T}}\boldsymbol{WA})^{-\boldsymbol{1}}\boldsymbol{A}^{\boldsymbol{T}}\boldsymbol{Wp}$, where $\boldsymbol{W}$ is a diagonal matrix whose diagonal elements are the weights (Price et al., 2001).

The process of the LTD algorithm actually constructs a regularized inverse problem. It can be viewed as one special case of the well-known Tikhonov regularization technique. The Tikhonov $L_2$ regularization can be written as the following minimization problem (Gholami and Hosseini, 2013)

$$\min_{\boldsymbol{c}} \quad \|\boldsymbol{Lc} - \boldsymbol{b}\|_2^2 + \mu\|\boldsymbol{D}_k\boldsymbol{c}\|_2^2 \tag{6}$$

where the first term represents the discrepancy between the measured and predicated values, the second term is the regularization term adding a smoothness penalty to the solution, $\mu$ is the regularization parameter controlling the conditioning of the problem, matrix $\boldsymbol{D}_k$ is the regularization operator, which is typically a $k$th-order difference operator. The first- and the second-order difference operators are commonly used. We can see that the LTD algorithm uses the third-order forward difference operator

$$\boldsymbol{D}_3 = \begin{bmatrix} -1 & 3 & -3 & 1 & & & & \\ & -1 & 3 & -3 & 1 & & & \\ & & & \ddots & & & & \\ & & & 1 & 3 & -3 & 1 & \\ & & & & 1 & 3 & -3 & 1 \end{bmatrix} \frac{1}{\Delta d} \in \mathbb{R}^{(m-3)\times n} \tag{7}$$

For pixels on the edges, the second-order and first-order difference operators can be used. The regularization parameter is analog to the weight parameter for the prior equations in the LTD algorithm.

The regularization parameter determines the balance between data fidelity and regularization terms. Determination of optimum regularization parameter is an important step of the regularization method. However, the regularization parameter is problem and data dependent. There is no general-purpose parameter-choice algorithm which will always produce a good parameter. For simplicity, we use the method based on discrepancy principle (Hamarik et al., 2012). The regularization parameter $\mu$ is chosen from a finite section of a monotonic sequence. For each value of $\mu$, an optimal solution is derived by solving the inverse problem. Then the discrepancy can be calculated. The regularization parameter is determined to be the highest value that makes the discrepancy $\|\boldsymbol{Lc}-\boldsymbol{b}\|_2^2$ equal to $N_b\sigma^2$, where $\sigma$ is the standard deviation of the noise. In this study, the reconstructions varied only slowly with the regularization parameters. Therefore, precise selection of the parameter was not necessary. For computational efficiency, the regularization parameter was selected from four widely varying values. The one produced the smallest discrepancy was used.

### 2.3 Variational interpolation and minimum curvature algorithm

Splines are special types of piecewise polynomials, which have proved to be very useful in numerical analysis and have founded in many applications in science and engineering problems. They match given values at some points (called knots) and have continuous derivatives up to some order at these points (Champion et al., 2000). Spline interpolation is preferred over polynomial interpolation by fitting low-degree polynomials between each of the pairs of the data points instead of fitting a single high-degree polynomial. Normally, the spline functions can be found by solving a system of linear equations with unknown coefficients of the low-degree polynomials defined by the given boundary conditions.

The variational approach gives a new way to find the interpolating splines and opens up directions for theoretical developments and new applications (Champion et al., 2000). The variational interpolation was motivated by the minimum curvature property of natural cubic splines, i.e., the interpolated surface minimizes an energy functional which corresponds to a physical bending energy. This principle provides a lot of flexibility in controlling the behavior of the generated spline. Given an observation $z_k$ ($k$=1, …, $N$) measured at $k$-th point whose position vector is $\boldsymbol{r}_k$, a spline function $F(\boldsymbol{r})$ interpolating the data points can be found through variational approach by minimizing the sum of the deviation from the measured points and the smoothness seminorm of the spline function

$$\min_F \sum_{k=1}^{N} |F(\boldsymbol{r}_k)-z_k|^2 + \omega I(F) \quad (8)$$

where $\omega$ is a positive weight, $I(F)$ denotes the smoothness seminorm. The seminorm can be defined in various forms. The commonly used ones are the first, second, third derivatives or their combinations. The solution of the minimizing problem is spline functions, which can also be found by solving a Euler-Lagrange differential equation corresponding to the given seminorm (Briggs, 1974).

We can see that the minimizing problem of Eq. (8) has a similar form to the Tikhonov regularization, but with a more flexible regularization term. The problem is that the variational interpolation is based on given data points, while the tomographic reconstruction is based on measured line integrals. However, we show in this study that the variational approach for interpolation can also be applied to the latter problem to produce a smoothness solution having similar effect of spline interpolation. Also, based on different seminorms, we can formulate many different reconstruction algorithms. In this way, a new minimum curvature (MC) algorithm was proposed in this study.

Assuming the unknown concentration distribution is described by a function $f(x,y)$, $(x_k, y_l)$ is the lowest coordinates of the $j$-th pixel at row $k$ and column $l$ of the 2-D grids, then the concentration $c_j$ equals to the average concentration of the pixel

$$c_j = \frac{1}{(\Delta d)^2}\int_{x_k}^{x_{k+1}}\int_{y_l}^{y_{l+1}} f(x,y)dxdy \tag{9}$$

The minimization problem according to the variational approach is formulated as

$$\min_{f}\ \sum_{i=1}^{N_b}\sum_{j=1}^{N_c} || L_{ij}c_j - b_i||_2^2 + \ \omega I(f) \tag{10}$$

For MC algorithm, we define seminorm according to the minimum curvature approach, which is used in the geographic data interpolation to seek a 2-D surface having continuous second derivatives and minimal total squared curvature (Briggs, 1974). The minimum-curvature surface has an analogy in elastic plate flexure and approximates the shape adopted by a thin plate flexed to pass through the observation data points with a minimum amount of bending. This method generates the smoothest possible surface while attempting to honor the observation data as closely as possible. The seminorm in the MC algorithm is defined to be equal the total square curvature

$$I(f) \ = \int\int\left(\frac{\partial^2 f}{\partial x^2}+\frac{\partial^2 f}{\partial y^2}\right)^2 dxdy \tag{11}$$

This integral needs to be discretized according to the grid division. The discrete total square curvature is

$$I = \sum_{k=1}^{n}\sum_{l=1}^{m}(I_{k,l})^2 \tag{12}$$

where $I_{k,l}$ is the curvature at the $(k,l)$ pixel, which is a function of $C_{k,l}$ and its neighboring pixel values. In two dimensions the approximation to the curvature is

$$I_{k,l} = (C_{k+1,l} + C_{k-1,l} + C_{k,l+1} + C_{k,l-1} - 4C_{k,l})/(\Delta d)^2 \tag{13}$$

To minimize the total squared curvature, we need

$$\frac{\partial I}{\partial C_{k,l}} = 0 \tag{14}$$

Combining Eq. (11), (12), and (13), we get the following difference equation

$$\begin{aligned}[C_{k+2,l} + C_{k,l+2} + C_{k-2,l} + C_{k,l-2}\\ +2(C_{k+1,l+1} + C_{k-1,l+1} + C_{k+1,l-1} + C_{k-1,l-1})\\ -8\left(C_{k+1,l} + C_{k-1,l} + C_{k,l-1} + C_{k,l+1}\right) + 20C_{k,l}]/(\Delta d)^2 \ = 0\end{aligned} \tag{15}$$

This equation is appended at each pixel as a smoothness regularization. Therefore, there is only one prior equation at each grid instead of two equations in the LTD algorithm. For pixels on the edges, we set the approximation of the first and second derivatives to be zeros. Assuming $\boldsymbol{M}$ is the kernel matrix of the prior equations, the reconstruction is to minimize the following problem

$$\min_{\boldsymbol{c}}\ ||\boldsymbol{Lc} - \boldsymbol{b}||_2^2 + \lambda||\boldsymbol{Mc}||_2^2, \text{ subject to } \boldsymbol{c} \geq 0 \tag{16}$$

where the parameter $\lambda$ is determined in the same way as determining the regularization parameter in the Tikhonov regularization method. Similar to the LTD approach, the resulted constrained system of linear equations is also over-determined and is solved by the NNLS optimization algorithm.

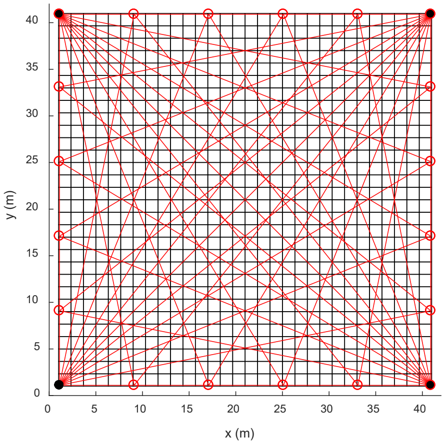

**Figure 2.** The Beam geometry and a 30 × 30 grid division of the site.

For conventional pixel-based reconstruction algorithms, the number of pixels (unknowns) should be no more than the number of beams (equations) in order to get a well-posed problem. Because only tens of beams are usually used in the ORS-CT applications, the resulted spatial resolution is very coarse. The GT algorithm is one way to increase the resolution. But it needs several steps to complete the whole translation because each translation uses a different grid division and the reconstruction process needs to be conducted for each grid division. In the MC algorithm, we use only one division of high-resolution grids directly during the reconstruction. The resulted system of linear equations is still determined because of the smoothness restriction at each pixel. As shown in Fig. 2, 30 × 30 pixels are used in the MC algorithm instead of the 6 × 6 pixels in the NNLS approach. Under this configuration, the number of linear equations for the LTD algorithms is approximately 38+30×30×2=1838. While the number for the MC algorithm is about 38+30×30 = 938. We can see that the MC approach reduced the number of linear equations by approximately half comparing to the LTD algorithm. The smoothness seminorm of the MC algorithm will guarantee a smooth solution. This smooth effect is similar to the spline interpolation applied after the reconstruction process, except that it is achieved during the inverse process. This is important because an interpolation after the reconstruction cannot correct the error resulting from the reconstruction based on coarse spatial resolution. While the MC approach evaluates the discrepancy based on the high-resolution values that are the same as the reconstruction outcomes. Errors due to coarse spatial resolution are corrected during the process.

…

## 2.5 Evaluation of reconstruction quality

…

In this paper, a measure using the resolution matrix is also used to predicate the reconstruction error due to different regularizations approaches. Resolution matrices are commonly used to determine whether model parameters can be independently predicted or resolved and how regularization limits reconstruction accuracy (Twynstra and Daun, 2012; von Clarmann et al., 2009). Ignoring the non-negative constrains, the generalized inverse matrices for the NNLS, LTD, and MC algorithms can be found by

$$\boldsymbol{G}_{NNLS} = (\boldsymbol{L}^T\boldsymbol{L})^{-1}\boldsymbol{L}^T$$

$$\boldsymbol{G}_{LTD} = (\boldsymbol{L}^T\boldsymbol{L} - \mu^2\boldsymbol{D}_3^T\boldsymbol{D}_3)^{-1}\boldsymbol{L}^T$$

$$\boldsymbol{G}_{MC} = (\boldsymbol{L}^T\boldsymbol{L} - \lambda^2\boldsymbol{M}^T\boldsymbol{M})^{-1}\boldsymbol{L}^T \qquad (21)$$

The resolution matrix is defined as $\boldsymbol{R}$=$\boldsymbol{GL}$. The reconstruction error is given by

$$\delta\boldsymbol{c} = \boldsymbol{c}_{\boldsymbol{model}} - \boldsymbol{c}_{\boldsymbol{exact}} = (\boldsymbol{R} - \boldsymbol{I})\boldsymbol{c}_{\boldsymbol{exact}} - \boldsymbol{G}\delta\boldsymbol{b} \qquad (22)$$

where $\boldsymbol{c}_{model}$, $\boldsymbol{c}_{exact}$ is the model-predicated and the exact concentrations respectively, $\delta\boldsymbol{b}$ is the perturbation of the observation, $\boldsymbol{I}$ is the identity matrix, $(\boldsymbol{R} - \boldsymbol{I})\boldsymbol{c}_{\boldsymbol{exact}}$ is the regularization error caused by the inconsistency between the measurement data equations and the prior information equations, $\boldsymbol{G}\delta\boldsymbol{b}$ is the perturbation error.

For the LTD and MC approaches using high-resolution grids, the kernel matrix $\boldsymbol{L}$ is rank-deficient, and the regularized solution is robust to perturbation error over a wide range of regularization parameter. Thus, the perturbation error is negligible, and the reconstruction error is dominated by regularization error (Twynstra and Daun, 2012). Because the resolution matrix is only determined by the beam configuration and the regularization approach, it is independent of the actual concentration distribution. Due to this reason, it is better to be used to evaluate different beam configurations which have considerable influence on the reconstruction accuracy. However, in this study the beam configurations are fixed. We can therefore use the resolution matrix to measure different regularization approaches. In an ideal experiment, $\boldsymbol{R}$=$\boldsymbol{I}$, which implies that each unknown pixel value can be independently resolved from the measurement data. The regularization term forces the off-diagonal terms in $\boldsymbol{R}$ to be nonzero, making the estimated concentration of each pixel a weighted average of the concentration of the surrounding pixels. We can use the Frobenius distance between $\boldsymbol{R}$ and $\boldsymbol{I}$ defining a measure of fitness to predicate the reconstruction error (Twynstra and Daun, 2012).

$$\varepsilon = \frac{\boldsymbol{1}}{\boldsymbol{N_c}}\|\boldsymbol{R} - \boldsymbol{I}\|_F^{\boldsymbol{2}} \qquad (23)$$

## 3 Results and discussions

…

### 3.5 Fitness

The contour plots of the resolution matrices for the LTD and MC algorithms are shown in Fig. 4. (a) and (b). The fitness values are 1.4411 and 1.3878 for the LTD and MC algorithm respectively. The MC algorithm shows slightly better performance. The off-diagonal elements are not zeros. The reconstructed concentration at each pixel is a weighted average of the concentrations of the surrounding pixels because of the smoothness regularization. Each row of the resolution matrix can be regarded as smoothing weights. As the pixels have a 2-D arrangement, we show the 2-D display of the row of the 106th pixel (row and column indices are 4,16 in 2-D pixels) in the resolution matrix for the LTD and MC algorithms in Fig. 4. (c) and (d) as an example, from which we clearly see the dependence on the beam geometry. In this study, the beam configuration is fixed, thus the difference between the fitness values is mainly due to the use of different regularization approaches. The fitness difference between the LTD and MC algorithms is very small, which may indicate that they have similar smoothness effects. This result coincides with results from other measures discussed above. The 2-D display of the diagonal elements of the resolution matrix are shown in Fig. 4. (e) and (f), which are not much useful in this case.

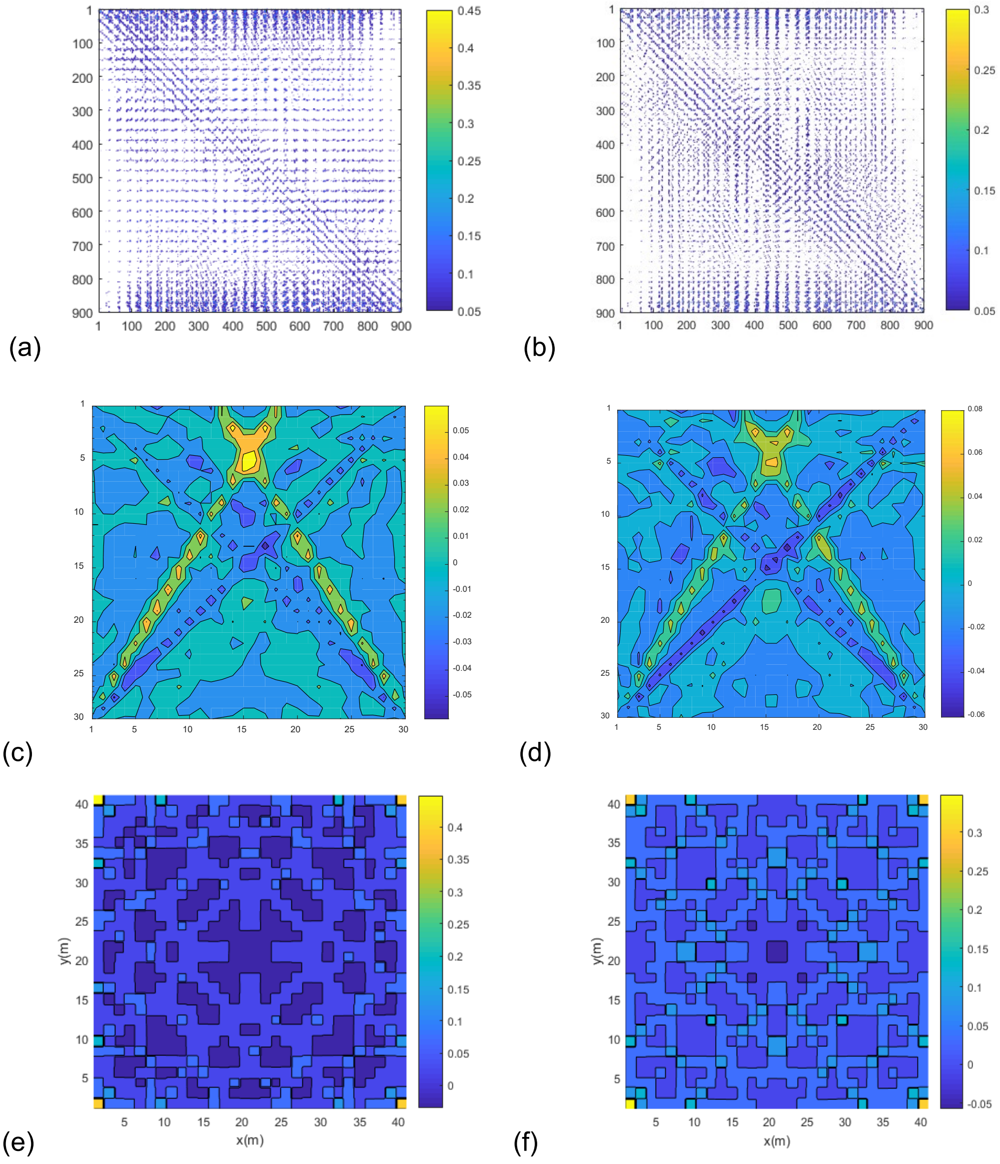

**Figure 4.** Contour plot of the resolution matrix for (a) the LTD algorithm (b) the MC algorithm. 2-D display of the row vector of the 106th pixel in the resolution matrix for (c) the LTD algorithm (d) the MC algorithm. 2-D display of the diagonal elements of the resolution matrix for (e) the LTD algorithm (f) the MC algorithm.

### 3.6 Influence of the grid size

The derivatives are approximated by the finite differences during the discretization process. The finite grid length causes discretization error and affects the reconstruction results. We studied the influences of different grid divisions by investigating the changes of the nearness, peak location error, exposure error, and computation time with respect to the pixel number. Five different grid divisions were used: 6 × 6, 12 × 12, 18 × 18, 24 × 24, and 30 × 30. The peak number was five. 100 maps were tested for each grid division. The results of the averaged values are shown in Fig. 5.

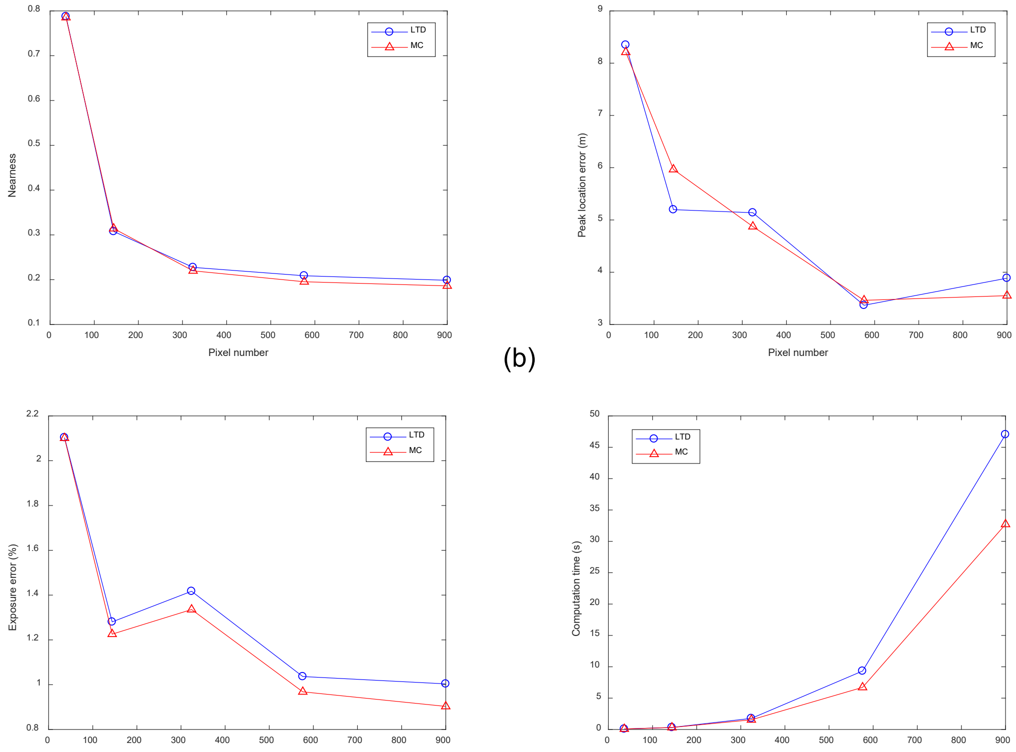

(a) (b)

(c) (d)

**Figure 5**. The change of (a) nearness (b) peak location error (c) exposure error percentage (d) computation time with respect to the pixel number.

We can see that the nearness, peak location error, and exposure error generally illustrate decreasing trends with the increase of the pixel number. The MC algorithm shows slightly better performance than the LTD algorithm with the increase of the pixel number. The performance improvements become slow for both algorithms when the division is finer than 24 × 24. On the other hand, the computation time shows approximately exponential growth trend with the increase of the pixel number. The LTD algorithm has a faster increasing rate than the MC algorithm. To conclude, the reconstruction performances are improved for both LTD and MC algorithms with the increase of the pixel numbers, but at the cost of exponential growth of the computation time. And the improvement becomes small when the resolution is higher than certain threshold value (24×24 in this study). So there should be a balance between the performance and the computation time.

…

## References

Arghand, T., Karimipanah, T., Awbi, H.B., Cehlin, M., Larsson, U., Linden, E.: An experimental investigation of the flow and comfort parameters for under-floor, confluent jets and mixing ventilation systems in an open-plan office. Building and Environment, 92, 48-60. DOI: 10.1016/j.buildenv.2015.04.019, 2015.

Belotti, C., Cuccoli, F., Facheris, L., Vaselli, O.: An application of tomographic reconstruction of atmospheric CO2 over a volcanic site based on open-path IR laser measurements. IEEE Transactions on Geoscience and Remote Sensing, 41:11, 2629-2637. DOI: 10.1109/TGRS.2003.815400, 2003.

Briggs, I.C.: Machine contouring using minimum curvature. Geophysics, 39:1, 39. DOI: 10.1190/1.1440410, 1974.

Cehlin, M.: Mapping tracer gas concentrations using a modified Low Third Derivative method: numerical study. International Journal of Ventilation, 18:2, 136-151. DOI: 10.1080/14733315.2018.1462935, 2019.Drescher, A.C., Gadgil, A.J., Price, P.N., Nazaroff, W.W.: Novel approach for tomographic reconstruction of gas concentration distributions in air: Use of smooth basis functions and simulated annealing. Atmospheric Environment, 30:6, 929–940. DOI: 10.1016/1352-2310(95)00295-2, 1996.

Censor, Y.: Finite series-expansion reconstruction methods. Proceedings of the IEEE, 71:3, 409-419. DOI: 10.1109/PROC.1983.12598, 1983.

Champion, R., Lenard, C. T., Mills, T. M.: A variational approach to splines. The ANZIAM Journal, 42:1, 119-135. DOI: 10.1017/S1446181100011652, 2000.

von Clarmann, T., De Clercq, C., Ridolfi, M., Hoepfner, M., and Lambert, J.-C.: The horizontal resolution of MIPAS, Atmos. Meas. Tech., 2, 47–54, https://doi.org/10.5194/amt-2-47-2009, 2009.

Du, K., Rood, M. J., Welton, E. J., Varma, R. M., Hashmonay, R. A., Kim, B. J., Kemme, M. R.: Optical Remote Sensing to Quantify Fugitive Particulate Mass Emissions from Stationary Short-Term and Mobile Continuous Sources: Part I. Method and Examples. Environ. Sci. & Technol., 45, 658-665. DOI: 10.1021/es101904q, 2011.

EPA: Measurement of Fugitive Emissions at a Landfill Practicing Leachate Recirculation and Air Injection. EPA-600/R-05/088, 2005.

Gholami, A., Hosseini, M.: A balanced combination of Tikhonov and total variation regularizations for reconstruction of piecewise-smooth signals. Signal Processing, 93:7, 1945-1960. DOI: 10.1016/j.sigpro.2012.12.008, 2013.

Giuli, D., Facheris, L., Tanelli, S.: Microwave tomographic inversion technique based on stochastic approach for rainfall fields monitoring. IEEE Transactions on Geoscience and Remote Sensing, 37, 5, 2536-2555. DOI: 10.1109/36.789649, 1999.

Hamarik, U., Palm, R., Raus, T. A family of rules for parameter choice in Tikhonov regularization of ill-posed problems with inexact noise level. Journal of Computational and Applied Mathematics, 236:8, 2146-2157. DOI: 10.1016/j.cam.2011.09.037, 2012.

Hashmonay, R.A., Natschke, D.F., Wagoner, K., Harris, D.B., Thompson, E.L, Yost, M.G.: Field Evaluation of a Method for Estimating Gaseous Fluxes from Area Sources Using Open-Path Fourier Transform Infrared. Environ. Sci. Technol., 35:11, 2309-2313. DOI: 10.1021/es0017108, 2001.

Hashmonay, R.A., Yost, M.G., Wu, C.F.: Computed tomography of air pollutants using radial scanning path-integrated optical remote sensing. Atmospheric Environment, 33, 267-274. DOI: 10.1016/S1352-2310(98)00158-7, 1999.

Hashmonay, R.A.: Theoretical evaluation of a method for locating gaseous emission hot spots. Journal of the Air and Waste Management Association, 58:8, 1100-1106. DOI: 10.3155/1047-3289.58.8.1100, 2012.

Herman, G. T.: Fundamentals of computerized tomography: Image reconstruction from projection, 2nd edition, Springer, 2009.

Lawson, C.L., Janson, R.J.: Solving least squares problems. Society for Industrial and Applied Mathematics: Philadelphia, 23, 158-165. DOI: 10.1137/1.9781611971217, 1995.

Twynstra, M. G., Daun, K. J.: Laser-absorption tomography beam arrangement optimization using resolution matrices. Applied Optics 51:29,7059-7068. DOI: 10.1364/AO.51.007059, 2012.

Mitasova, H., Mitas, L., Brown, W.M., Gerdes, D.P., Kosinovsky, I., Baker, T.: Modelling spatially and temporally distributed phenomena: new methods and tools for GRASS GIS, International Journal of Geographical Information Systems, 9:4, 433-446. DOI: 10.1080/02693799508902048, 1995.

Price, P.N., Fischer, M.L., Gadgil, A.J., Sextro, R.G.: An algorithm for real-time tomography of gas concentrations, using prior information about spatial derivatives. Atmos. Environ., 35, 2827. DOI: 10.1016/S1352-2310(01)00082-6, 2001.

Radon, J., On the determination of functions from their integral values along certain manifolds. IEEE transactions on medical imaging, **5**:4: 170-176, 1986.

Rudin, L., Osher, S.J., Fatemi, E.: Non-linear total variation based noise removal algorithms. Physica D, 60, 259–268.

Samanta, A., Todd, L.A., 2000. Mapping chemicals in air using an environmental CAT scanning system: evaluation of algorithms. Atmospheric Environment, 34, 699-709. DOI: 10.1016/S1352-2310(99)00331-3, 1992.

Tikhonov, A.N., Arsenin, V.Y.: Solutions of Ill-posed Problems, Winston and Sons, Washington, 1977.

Todd L., Ramachandran, G.: Evaluation of Optical Source-Detector Configurations for Tomographic Reconstruction of Chemical Concentrations in Indoor Air, American Industrial Hygiene Association Journal, 55:12, 1133-1143, DOI: 10.1080/15428119491018204, 1994.

Tsui, B.M.W., Zhao, X., Frey, E.C., Gullberg, G.T.: Comparison between ML-EM and WLS-CG algorithms for SPECT image reconstruction. IEEE Transactions on Nuclear Science, 38:6, 1766-1772. DOI: 10.1109/23.124174, 1991.

Verkruysse, W., Todd L.A.: Improved method "grid translation" for mapping environmental pollutants using a two-dimensional CAT scanning system. Atmospheric Environment, 38, 1801–1809. DOI: 10.1016/j.sigpro.2012.12.008, 2004.

Verkruysse, W., Todd, L.A.: Novel algorithm for tomographic reconstruction of atmospheric chemicals with sparse sampling. Environ Sci Technol., 39:7, 2247-2254. DOI: 10.1021/es035231v, 2005.

Wu, C.F., Chang, S.Y.: Comparisons of radial plume mapping algorithms for locating gaseous emission sources. Atmospheric Environment, 45, 1476-1482. DOI: 10.1016/j.atmosenv.2010.12.016, 2011.

Wu, C.F., Yost, M.G., Hashmonay, R.A., Park, D.Y.: Experimental evaluation of a radial beam geometry for mapping air pollutants using optical remote sensing and computed tomography. Atmospheric Environment, 33, 4709-4716. DOI: 10.1016/S1352-2310(99)00218-6, 1999.